Synthesis of a NiMoO$_4$/3D-rGO Nanocomposite via Starch Medium Precipitation Method for Supercapacitor Performance

Shahrzad Arshadi Rastabi [1] , **Rasoul Sarraf Mamoory [1],*** , **Nicklas Blomquist [2]**, **Manisha Phadatare [2] and Håkan Olin [2]**

[1] Department of Materials Engineering, Tarbiat Modares University, 14115111 Tehran, Iran; Shahrzad.Arshadi@modares.ac.ir

[2] Department of Natural Sciences, Mid Sweden University, 85170 Sundsvall, Sweden; Nicklas.Blomquist@miun.se (N.B.); Manisha.Phadatare@miun.se (M.P.); Hakan.Olin@miun.se (H.O.)

* Correspondence: rsarrafm@modares.ac.ir; Tel.: +98-912-133-4979

Abstract: This paper presents research on the synergistic effects of nickel molybdate and reduced graphene oxide as a nanocomposite for further development of energy storage systems. An enhancement in the electrochemical performance of supercapacitor electrodes occurs by synthesizing highly porous structures and achieving more surface area. In this work, a chemical precipitation technique was used to synthesize the NiMoO$_4$/3D-rGO nanocomposite in a starch media. Starch was used to develop the porosities of the nanostructure. A temperature of 350 °C was applied to transform graphene oxide sheets to reduced graphene oxide and remove the starch to obtain the NiMoO$_4$/3D-rGO nanocomposite with porous structure. The X-ray diffraction pattern of the NiMoO$_4$ nano particles indicated a monoclinic structure. Also, the scanning electron microscope observation showed that the NiMoO$_4$ NPs were dispersed across the rGO sheets. The electrochemical results of the NiMoO$_4$/3D-rGO electrode revealed that the incorporation of rGO sheets with NiMoO$_4$ NPs increased the capacity of the nanocomposite. Therefore, a significant increase in the specific capacity of the electrode was observed with the NiMoO$_4$/3D-rGO nanocomposite (450 Cg^{-1} or 900 Fg^{-1}) when compared with bare NiMoO$_4$ nanoparticles (350 Cg^{-1} or 700 Fg^{-1}) at the current density of 1 A g^{-1}. Our findings show that the incorporation of rGO and NiMoO$_4$ NP redox reactions with a porous structure can benefit the future development of supercapacitors.

Keywords: electrochemical performance; starch; porous structure; NiMoO$_4$/3D-rGO nanocomposite; NiMoO$_4$ NPs

1. Introduction

Green energy plays a key role in the development of modern human life and the advancement of new technologies. Electrochemical energy storage (EES) systems like batteries and supercapacitors are among the various energy storage systems that have received great attention currently. Supercapacitors, in particular, have generated great interest due to their high power density and long cycling life [1]. Better performance of the electrodes can be achieved by the development and modification of the new materials [2]. Generally, three types of electrode materials—carbon materials, metal oxide, and conducting polymers—have been used for supercapacitors [3]. However, transition metal oxides and hydroxides, such as NiO [4], Ni(OH)$_2$ [5–7], MnO$_2$ [8,9], MoO$_3$ [10], and Co$_3$O$_4$ [11], are mostly employed as the supercapacitors material. These types of electrode materials are low cost and naturally abundant, with significant specific capacity based on redox reactions and high electrochemical activity [12]. Lately, binary metal oxides such as NiCo$_2$O$_4$ [13], NiMoO$_4$ [14,15], CoMoO$_4$ [16],

and MnMoO$_4$ [17] have attracted significant attention as good candidates for supercapacitors. Binary metal oxides present different oxidation states and significantly higher electrical conductivity than single metal oxides. Among these binary metal oxides, NiMoO$_4$ has attracted significant research interest because of the high electrical conductivity of the Mo element and the high electrochemical activity attributed to rich redox reactions of the nickel ions [18]. Most of the articles on NiMoO$_4$ has adopted the theory of a pseudocapacitive charge storage mechanism, but a few recent articles have treated the material as battery-like. There seems to be theories in contradiction in this field. However, since this study does not focus on the specific charge storage mechanism, along with the references, we have adopted the theory of pseudocapacitive behavior. In addition, NiMoO$_4$ nanoparticles (NPs) are readily available and highly stable in alkaline electrolytes [19]. Furthermore, hybridizing metal oxides with carbon materials can be an effective method to improve the electrical conductivity and the performance of the supercapacitors [20]. This encouraged us to fabricate reduced graphene oxide (rGO) and NiMoO$_4$ nanocomposite with a unique nanostructure, which will combine the advantages of both rGO with low electrical resistance and the quick redox reactions of NiMoO$_4$.

Various synthesis methods have been studied to produce the NiMoO$_4$ nanostructures, such as co-precipitation [21], sol-gel [14], microwave-assisted solvothermal [22], sonochemical [23], microwave sintering [24], and hydrothermal [25] methods. In this work, we propose a facile and an efficient method to synthesize a new three-dimensional hybrid structure, combining NiMoO$_4$ NPs and rGO. This method can produce large amounts of material with less equipment and low temperatures compared to other techniques. However, the highly porous structure is the key parameter in supercapacitors, and a comprehensive report on the synthesis of such porous NiMoO$_4$/3D-rGO nanostructures by a facile method is lacking. Therefore, starch was used in this study during the preparation of the nanocomposite by a simple precipitation method to gain porosity and surface area. The porous structure provides a rapid ion diffusion path and increases the capacity.

2. Experimental

2.1. Materials

Sodium molybdate dihydrate (Na$_2$MoO$_4$·2H$_2$O), nickel nitrate hexahydrate (Ni(NO$_3$)$_2$·6H$_2$O), graphene oxide (GO), and potassium hydroxide (KOH) were provided from Merck, Sundsvall, Sweden. Polyvinylidene fluoride (PVDF), dimethylformamide (DMF), and starch ((C$_6$H$_{10}$O$_5$)$_n$) were purchased from Sigma-Aldrich, Sundsvall, Sweden. In addition, distilled water was used throughout the sample preparation.

2.2. Synthesis of NiMoO$_4$ Nanoparticles and NiMoO$_4$ NPs/rGO Nanocomposite

The NiMoO$_4$ NPs/rGO nanocomposite was produced with a chemical precipitation method. At first, a solution of starch was prepared at 80 °C (containing 1 g of starch in 20 mL of H$_2$O). Then, 1 mg of GO was added to the prepared starch solution. Next, 20 mL of 50-mM Ni(NO$_3$)$_2$·6H$_2$O and 20 mL of 50-mM Na$_2$MoO$_4$·2H$_2$O were prepared separately at room temperature. Following this, Ni(NO$_3$)$_2$·6H$_2$O was first added to the mixed solution of starch/GO, and after 10 min of stirring through a magnetic stirrer, 50-mM Na$_2$MoO$_4$·2H$_2$O was added to the above solution with continued stirring for 1 h at the temperature of 80 °C. The products were collected by centrifugation at 8000 rpm and distilled water was used to wash the prepared powder, and then a vacuum oven with a temperature of 60 °C was applied to dry the samples for 24 h. Finally, the as-prepared powder was annealed at the temperature of 350 °C for 2 h in an Ar atmosphere to produce the NiMoO$_4$/3D-rGO nanocomposite. The same experiment without adding GO was performed to prepare pure NiMoO$_4$ NPs.

2.3. Fabrication of NiMoO$_4$ NPs and NiMoO$_4$/3D-rGO Nanocomposite Electrodes

For the electrochemical study, the Ni foam surface was first washed repeatedly with HCl (37 wt.%) and ethanol. The electrodes were fabricated by mixing an electroactive material (NiMoO$_4$

or NiMoO$_4$/3D-rGO-80 wt.%), carbon black (10 wt.%), and PVDF (10 wt.%) in DMF as the solvent. The mixture was subjected to intense ultrasonic treatment for 10 min to form a homogeneous paste. The final mixture was mechanically pasted on the Ni foam surface (1 × 1 cm^2) and dried at 70 °C for 12 h. The active mass loading on the Ni foam surface was estimated to be 2 mg·cm^{-2} for each electrode.

2.4. Material Characterization

The prepared powder was characterized using several analytical systems. Powder X-ray diffraction (XRD, Bruker D2 Phaser, Cu K$_\alpha$ radiation, Sweden) was used to investigate the composition of the as-prepared samples. The morphology and microstructure of the powder were characterized using field emission scanning electron microscopy (SEM assisted with Energy Dispersive X-ray Analysis (EDX), TESCAN MAIA3-2016, operated at 10.0 kV, Sweden). Raman spectroscopy (Horiba Xplora plus, laser excitation at 532 nm-frequency range of 50 to 3000 cm^{-1}) and Fourier transform infrared spectrometry (FTIR, ABB Bomem System-KBr method, Sweden-frequency range of 400 to 4000 cm^{-1}) were also used for the identification of molecular bonding.

2.5. Electrochemical Characterization

The electrochemical properties of NiMoO$_4$ NPs and NiMoO$_4$/3D-rGO electrodes were evaluated with three-electrode cells in a 3 M-KOH electrolyte with the potentiostat system (VersaStat 4 with VersaStudio, Sundsvall, Sweden). A reference electrode (saturated Hg/Hg$_2$Cl$_2$) and platinum (counter electrode) were used for supercapacitor measurement.

The electrochemical properties of the NiMoO$_4$ NPs and NiMoO$_4$/3D-rGO hybrid nanocomposite were characterized using cyclic voltammetry (CV), galvanostatic charge–discharge (GCD), and continuous charge–discharge tests. According to the battery-like behaviour of the Ni-based materials, calculation of the capacity (Cg^{-1}) is the true assessment of energy stored on such electrodes, rather than the capacitance with the unit of Fg^{-1} [7]. The specific capacity of the electrodes can be obtained from the discharge time of both cyclic voltammetry curves and the galvanostatic charge/discharge curves, according to the following equations [7]:

$$Q_{CV} = \frac{1}{mv} \int IdV, \tag{1}$$

$$Q_{GCD} = \frac{\int Idt}{m}, \tag{2}$$

where Q (Cg^{-1}) is the charge stored [7], I (A) refers to the discharge current, Δt (s) is attributed to the discharge time, and m (g) is related to the mass loading of the active material on the current collector [26,27].

3. Results and Discussion

3.1. Investigation of Morphology and Structural Characterization

FTIR spectral analysis was performed to investigate the chemical bonds of the produced samples and reduction of GO during the process. Figure 1 illustrates the FTIR spectra of the pure GO, NiMoO$_4$ NPs, and NiMoO$_4$/3D-rGO nanocomposite. The FTIR spectrum of GO showed a characteristic peak of C=O corresponding to stretching vibrations from a carbonyl group at ~1765 cm^{-1}. The bond at ~1650 cm^{-1} was attributed to the stretching of aromatic C=C bonds and the peaks at ~1397 cm^{-1}, ~1208 cm^{-1}, and ~1038 cm^{-1} corresponded to the C–OH and the deformation of C–O–C and C–O bonds, respectively [28,29]. As can be seen, the FTIR spectrum containing a broad bond between ~2800 and ~3600 cm^{-1} was due to the hydroxyl (O–H) stretching vibration mode of water molecules adsorbed on the surface of the samples [30]. The bonds before 1000 cm^{-1} were related to metal oxides. The characteristic bonds of NiMoO$_4$ appearing at 444 cm^{-1} and 750 cm^{-1} were assigned to Mo–O–Mo

and Mo–O–Ni vibrations, respectively. The bond appearing at 836 cm^{-1} can be attributed to the symmetric stretching of Mo=O bond [24]. As can be seen in the FTIR spectrum of NiMoO$_4$/3D-rGO nanocomposite, most of the oxygenated groups, like C–OH, C–O, and C=O, disappeared from the FTIR spectrum of the NiMoO$_4$/3D-rGO nanocomposites and C–O–C peak was weakened. This means that GO sheets were reduced to rGO, during the attraction of Ni^{2+} to the oxygen groups of GO with a negative charge [31]. In addition, the reduction of the strong absorption peak at 3150 cm^{-1} demonstrated the successful chemical reaction between graphene oxide and NiMoO$_4$ to form the NiMoO$_4$/3D-rGO nanocomposite.
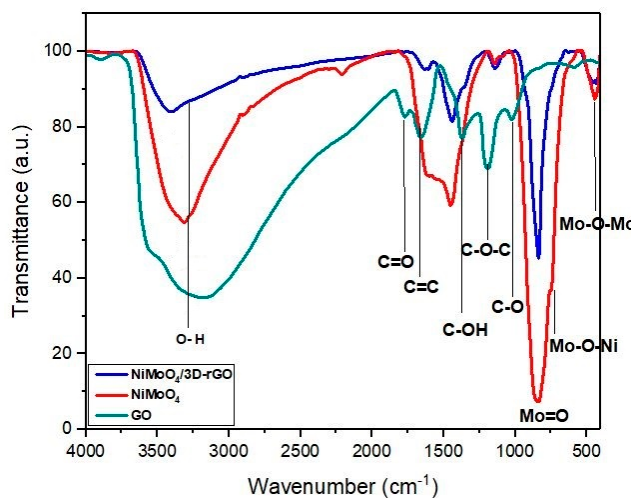
Figure 1. Fourier transform infrared spectrometry (FTIR) spectra of the graphene oxide (GO) sheets, NiMoO$_4$ nanoparticles (NPs), and NiMoO$_4$/3D-rGO nanocomposite.

X-ray powder diffraction analysis was performed to investigate the structure of the synthesized powders. In Figure 2, the XRD patterns of the NiMoO$_4$ NPs, NiMoO$_4$/3D-rGO nanocomposite, and pristine GO is illustrated. Diffraction peaks of the NiMoO$_4$ NPs in Figure 2a match with the code number of 00-045-0142. It should be noted that the peaks at around 27.3°, 30.36°, and 45° were attributed to α-NiMoO$_4$ [32]. During the process, Ni^{2+} and MoO$_4^{2-}$ cations reacted with OH$^-$ to form a Ni–Mo hydroxide precursor, as shown in the following equations [33]:

$$NO_3^- + 7H_2O + 8e^- \rightarrow NH_4^+ + 10OH^-, \tag{3}$$

$$Ni^{2+} + Mo^{6+} + 8OH^- \rightarrow NiMo(OH)_8, \tag{4}$$

$$NiMo(OH)_8 \rightarrow NiMoO_4 + 4H_2O. \tag{5}$$

Although the results indicate the presence of a dominant NiMoO$_4$ phase, small quantities of the orthorhombic Mo$_{17}$O$_{47}$ phase with a space group of Pba2 (JCPDS No. 01-071-0566) were also observed in the structure. The peaks at 2θ = 21.12° (510), 22.67° (001), and 32.07° (521) could be related to the Mo$_{17}$O$_{47}$ phase. It can be concluded that Mo$_{17}$O$_{47}$ phase consisted of 17 MoO$_3$ phases, which some of the oxygens replaced with vacancies, and finally Mo$_{17}$O$_{47}$ was formed instead of Mo$_{17}$O$_{51}$. In Figure 2b, the XRD pattern of the NiMoO$_4$/3D-rGO nanocomposite can be seen. No obvious peak related to GO (at 2θ = 10.6° (001) in Figure 2c) could be found in the XRD pattern of the NiMoO$_4$/3D-rGO nanocomposite. This confirms that the oxygen-containing functional groups of graphene oxide could be removed by reduction through NiMoO$_4$ NPs at 350 °C; furthermore, the rGO peaks did not appear in the XRD pattern of NiMoO$_4$/3D-rGO nanocomposite, which may be due to the lesser content of rGO and the strong NiMoO$_4$ NP peaks covering the rGO peaks [34,35]. Moreover, the distance between the graphene sheets was fully filled with the insertion of NiMoO$_4$ NPs into the interplanar groups [36].

Another reason for this is that carbon materials like rGO are amorphous and cannot be detected by X-ray diffraction.
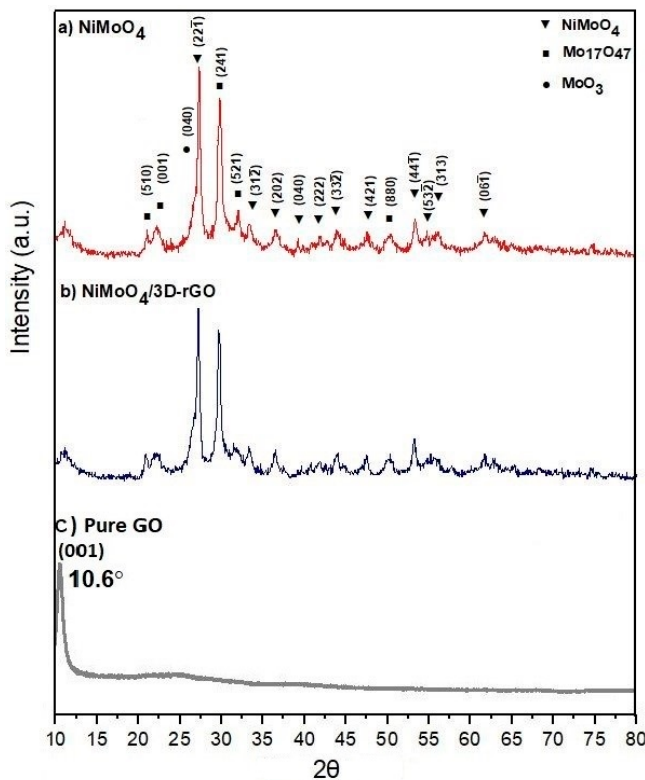
Figure 2. X-ray diffraction (XRD) patterns of the (**a**) NiMoO$_4$ NPs, (**b**) NiMoO$_4$/3D-rGO nanocomposite after heating at 350 °C, and (**c**) pristine GO.

In addition, the XRD pattern of the NiMoO$_4$ powder revealed an asymmetric peak at 2θ = 27.3°. For a more accurate study, this peak was opened. As shown in Figure 3, after deconvolution of the asymmetric peak, it was divided into two distinct peaks, at 2θ = 26.86° and 2θ = 27.31°. These peaks were respectively attributed to MoO$_3$ (040) and α-NiMoO$_4$ (221$^-$) phases. The MoO$_3$ phase was produced from a combination of Mo^{6+} ions and oxygen.
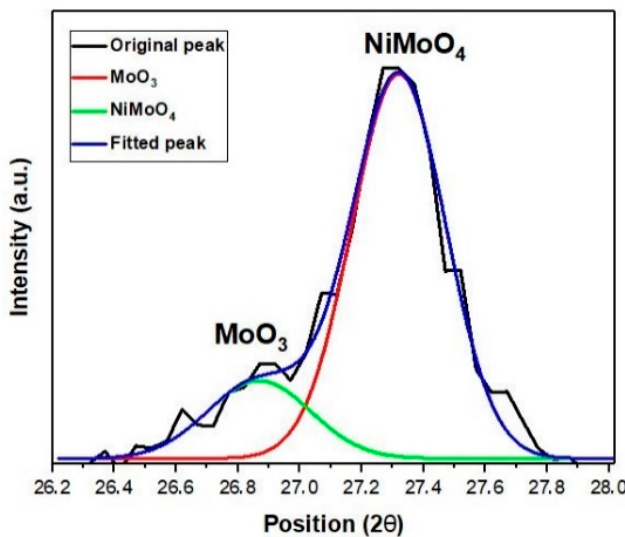
Figure 3. Deconvolution of asymmetric peak of the X-ray diffraction pattern of the NiMoO$_4$ nanopowder at 2θ = 27.3°.

The Raman spectra of GO, NiMoO$_4$ NPs, and NiMoO$_4$/3D-rGO nanocomposites (Figure 4) were analyzed to check whether GO was reduced during the synthesis. It was established from Figure 4a that GO had two characteristic peaks: the D bond at 1347 cm^{-1} originated from the defects in the hexagonal graphitic network and the G bond at 1584 cm^{-1} was due to the vibration of the sp^2 domain of carbon atoms [22]. Comparison of the Raman spectra of NiMoO$_4$/3D-rGO nanocomposite (Figure 4b) with GO spectra exhibited a shift in the D (1383.87 cm^{-1}) and G (1580.56 cm^{-1}) positions. The intensity ratio of the D and G peaks (I$_D$/I$_G$) reveals the degree of the disorders. By reduction of graphene oxide and removal of oxygen groups, the defects increased and the I$_D$/I$_G$ ratio showed an increase from 0.98 to 1.02. This was attributed to the increase of the defects in rGO [22,25,37]. The intensive peak at 969 cm^{-1}, and some slight intensity peaks at 928, 825, 394, and 325 cm^{-1} denoted the stoichiometric α-phase NiMoO$_4$ (Figure 4b,c) [32,38,39]. The peaks at 969 and 928 cm^{-1} were related to the symmetric and asymmetric stretching modes of the Mo=O bond, whereas the peak at 825 cm^{-1} occurred due to the Ni–O–Mo symmetric stretch. The peaks at 394 cm^{-1} and 325 cm^{-1} were representative of the bending band of Mo–O and Mo–O–O [32,37,40]. The Raman results confirmed the reduction of GO to rGO in the NiMoO$_4$/3D-rGO nanocomposite. Thus, by increasing the defects in rGO, more active sites can be provided for enhancing the electron storage and improvement of capacity [41].
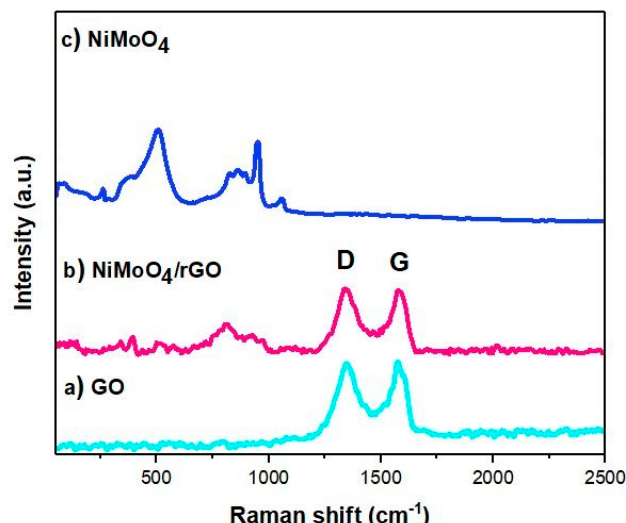
Figure 4. Raman spectrum of the GO, NiMoO$_4$, and NiMoO$_4$/3D-rGO nanocomposites.

Scanning electron microscopy (SEM) was performed to investigate the morphology and the porosities of the nanocomposite. The SEM images and EDX characterisation of the NiMoO$_4$ NPs and NiMoO$_4$/3D-rGO nanocomposite are illustrated in Figure 5. According to Figure 5a,b, NiMoO$_4$ NPs possess nanorod morphology with three-dimensional orientation and lots of porosities among the nanorods. To some extent, negligible agglomeration can be seen, which is related to the magnetic nature of NiMoO$_4$ [14]. Figure 5c,d demonstrates the decoration and dispersibility of the NiMoO$_4$ nanorods on the surface of rGO sheets. The attachment of metal ions to the functional group of GO sheets through electrostatic interactions resulted in the growth of NiMoO$_4$ NPs on the 3D reduced GO sheets [29,34]. Therefore, it can be stated that the rGO sheets play important roles as a useful site for the growth of NiMoO$_4$ NPs. The formation of porosities in the NiMoO$_4$/3D-rGO structure confirmed the transformation of starch to CO$_2$ and CO gases during the thermal process. The elemental compositions of the NiMoO$_4$ and NiMoO$_4$/3D-rGO samples were also analyzed by the energy dispersive X-ray method. Figure 5e,f shows the EDX spectra of NiMoO$_4$/3D-rGO and NiMoO$_4$ samples. The peaks confirm the presence of Ni, Mo, O, and C elements in the NiMoO$_4$/3D-rGO nanocomposite and Ni, Mo, and O elements in the NiMoO$_4$ spectrum.
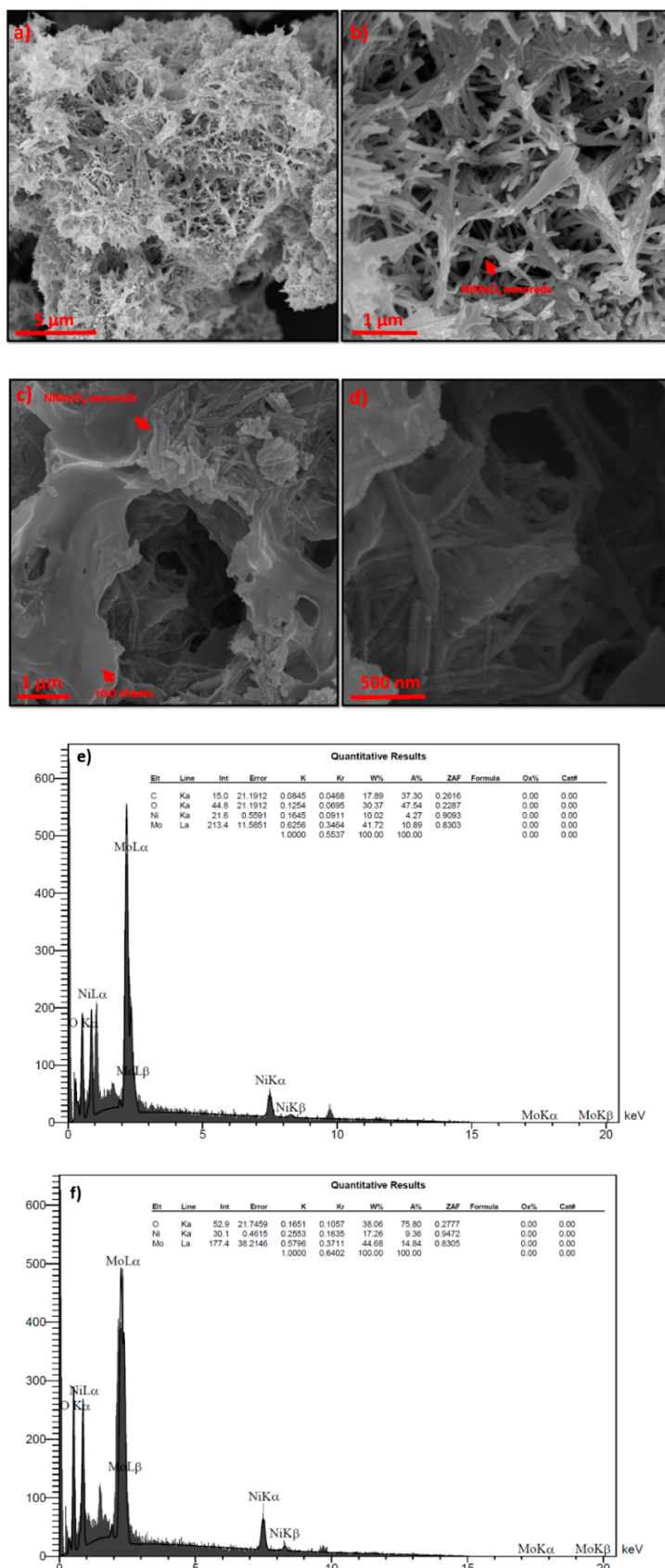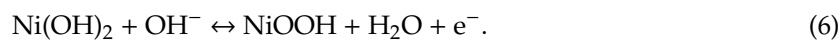
Figure 5. Scanning electron microscopy (SEM) images of (**a**,**b**) NiMoO$_4$ NPs with two different magnifications, (**c**,**d**) NiMoO$_4$/3D-rGO nanocomposite with various magnifications, (**e**) corresponding EDX spectra of NiMoO$_4$/3D-rGO, and (**f**) corresponding EDX spectra of NiMoO$_4$.

3.2. Electrochemical Measurement of the NiMoO$_4$ NPs and NiMoO$_4$/3D-rGO Electrodes

The potentiostat analysis system was used to explore the electrochemical performance of NiMoO$_4$ NPs and NiMoO$_4$/3D-rGO electrodes. Figure 6a and b show the CV curves of pure NiMoO$_4$ and NiMoO$_4$/3D-rGO electrodes. The working cell potential range of the electrodes was in the potential window of 0–0.7 V during the CV measurements at different scan rates from 10 to 100 mVs^{-1}. Figure 6a exhibits the CV patterns of NiMoO$_4$ NPs electrode. According to the curves, as the scan rate increased, the anodic and cathodic peaks moved towards the higher and lower potentials, respectively. This is related to the electrode internal resistance, which limits the charge transfer at high scan rates. At lower scan rates, a pair of redox peaks could be seen in each CV curve, indicating the Faradic reaction of Ni(II)/Ni(III) [26,42] due to the reversible phase change between Ni(OH)$_2$ and NiOOH (0.44 V and 0.18 V) [43]. By scanning the electrode, the OH$^-$ ions will be dispersed on the surface of Ni(OH)$_2$ layer and form the NiOOH phase, as shown in Equation (6):

$$Ni(OH)_2 + OH^- \leftrightarrow NiOOH + H_2O + e^-. \tag{6}$$

Mo is not involved in redox reactions. This element, with a high conductivity, can increase the whole capacity of the cell [26,44]. As shown in Figure 6b, the CV curves of the NiMoO$_4$/3D-rGO electrode, similar to the NiMoO$_4$ electrode (Figure 6a), at low scan rates displayed two redox peaks related to NiMoO$_4$ faradaic reactions (Ni^{2+}/Ni^{3+}). The NiMoO$_4$/3D-rGO hybrid electrode consisted of two mechanisms for storing energy: the faradaic reaction of NiMoO$_4$ as well as the formation of an electric double-layer because of the presence of the graphene oxide sheets in the composite. This can lead to the storage of more electrons in the NiMoO$_4$/3D-rGO in comparison to NiMoO$_4$. According to Equation (1), the maximum capacity for a NiMoO$_4$/3D-rGO electrode is 249.8 Cg^{-1} (356.4 Fg^{-1}) at a scan rate of 10 mVs^{-1} and at the scan rates of 20, 50, and 100 mVs^{-1}, it was calculated to be equal to 212.8 Cg^{-1} (304 Fg^{-1}), 152.95 Cg^{-1} (218.5 Fg^{-1}), and 84 Cg^{-1} (120 Fg^{-1}), respectively, whereas the calculated capacity for NiMoO$_4$ at the scan rates of 10, 20, 50, and 100 mVs^{-1} is 211.2 Cg^{-1} (301.7 Fg^{-1}), 192.85 Cg^{-1} (275.5 Fg^{-1}), 126.84 Cg^{-1} (181.2 Fg^{-1}), and 67.69 Cg^{-1} (96.7 Fg^{-1}). This shows that the introduction of rGO to NiMoO$_4$ increased the capacity. Figure 6c illustrates the CV curves of Ni foam, NiMoO$_4$ NPs, and the NiMoO$_4$/3D-rGO nanocomposite. As can be seen, the CV curve of the NiMoO$_4$/3D-rGO nanocomposite had a slightly larger enclosed area at the scan rate of 10 mV·s^{-1}, reflecting that the NiMoO$_4$/3D-rGO hybrid nanocomposite electrode has higher specific capacity and the Ni foam capacity can be neglected. More capacity of NiMoO$_4$/3D-rGO confirms that oxygenated functional groups of GO were removed and more conductivity provided, resulting in more capacity. In addition, the differences between the reduction and oxidation potentials for the NiMoO$_4$/3D-rGO and NiMoO$_4$ electrodes were 241 mV and 280 mV, respectively. Thnis reveals an improvement in the electrochemical reversibility of the NiMoO$_4$/3D-rGO electrode due to the addition of rGO sheets to NiMoO$_4$ NPs.

The galvanostatic charge–discharge (GCD) measurements were carried out at different current densities (1–50 A g^{-1}) and the potential range of 0–0.5 V for NiMoO$_4$ NPs and NiMoO$_4$/3D-rGO electrodes (Figure 6d,e). A pair of voltage plateaus as well as nonlinear curves of the GCD graphs confirm the faradaic redox reaction of Ni^{2+}/Ni^{3+} ions of the electrodes [45]. The NiMoO$_4$/3D-rGO electrode exhibited a specific capacity of 100 Cg^{-1} (200 Fg^{-1}) at the high current density of 10 A g^{-1}, whereas the specific capacity of pure NiMoO$_4$ NPs was 80.2 Cg^{-1} (160.4 Fg^{-1}) at 10 A g^{-1}.

Stability over repeated charge and discharge cycles is a critical parameter for supercapacitors. The cyclability of NiMoO$_4$ and NiMoO$_4$/3D-rGO electrodes was tested by continuous charge–discharge measurements (Figure 6f) over 400 cycles (24 h) at the current density of 2 A g^{-1} in 3M-KOH aqueous solution as an electrolyte. As shown in Figure 6f, increasing the number of cycles from 1 to 400 resulted in a reduction in the specific capacity of the NiMoO$_4$ electrode from 314.8 Cg^{-1} (629.6 Fg^{-1}) to 179.4 Cg^{-1} (358.8 Fg^{-1}). The specific capacity decreased during the first several cycles, then it remained stable at approximately 179.4 Cg^{-1} (358.8 Fg^{-1}), losing less than 57% capacity by the end of the test. The capacity of the NiMoO$_4$/3D-rGO electrode decreased with the increase in the cycle

number, which can be related to the decrease in the electroactive sites. Then, the specific capacity remained stable for the next cycles. In the end, approximately 41% of the initial capacity was still maintained. Electrochemical measurements showed that specific capacity of both electrodes reached around 160 Cg^{-1} (320 Fg^{-1}) at the current density of 2 A g^{-1} after 24 h. It can be concluded that the nanorod morphology of the NiMoO$_4$ and the porous structure facilitate better penetration and migration through the electrode surface path.
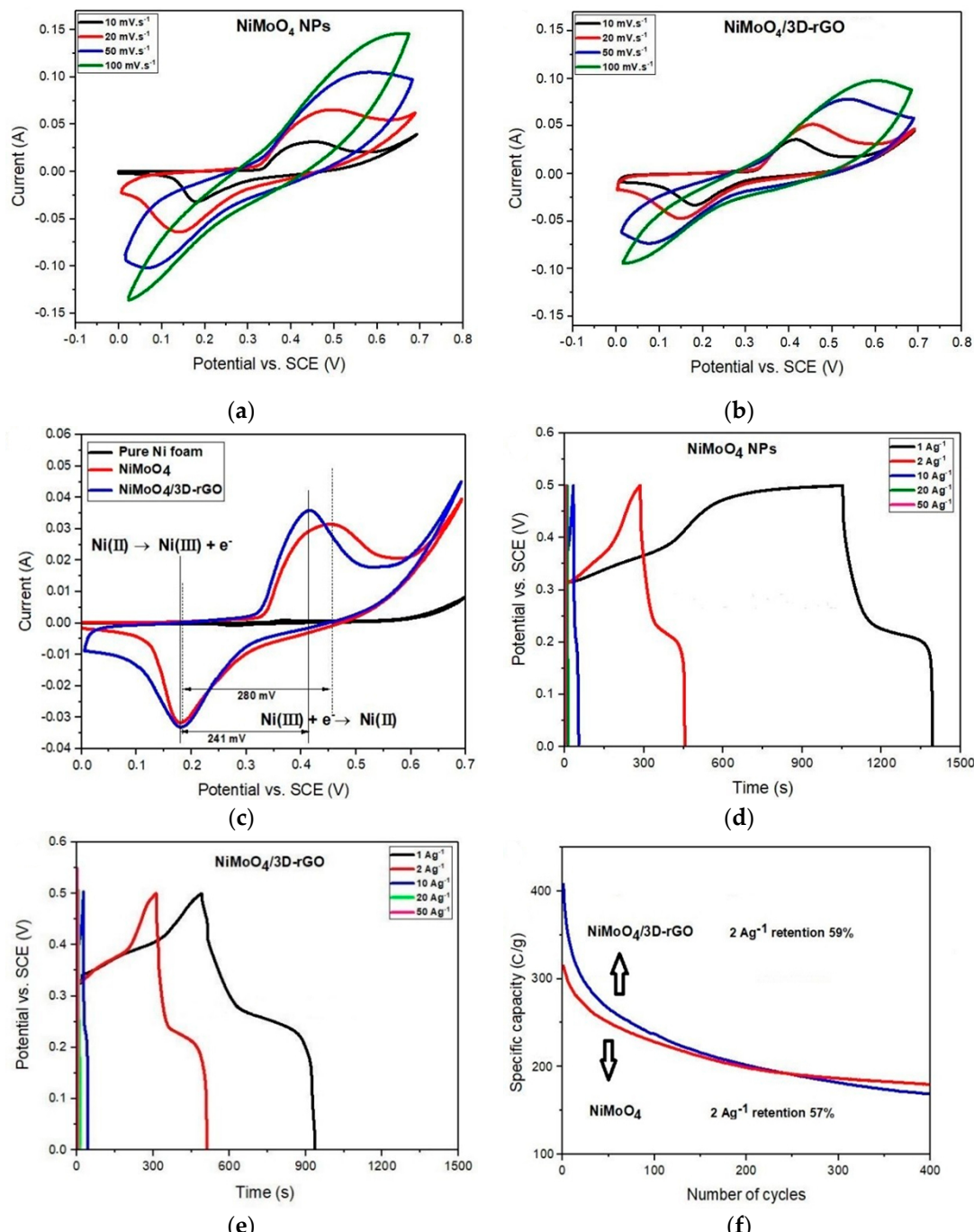
Figure 6. Cyclic voltametry curves of (**a**) pure NiMoO$_4$ NP electrode and (**b**) hybrid NiMoO$_4$/3D-rGO electrode at various scan rates (10–100 mV·s^{-1}); (**c**) CV curves of Ni foam, NiMoO$_4$ NPs, and NiMoO$_4$/3D-rGO electrode (10 mV·s^{-1}); Galvanostatic charge discharge curves of (**d**) pure NiMoO$_4$ NPs electrode and (**e**) hybrid NiMoO$_4$/3D-rGO electrode at different current densities (1–50 A g^{-1}); (**f**) age test of hybrid NiMoO$_4$/3D-rGO and pure NiMoO$_4$ NPs electrode at a current density of 2 A g^{-1}.

The capacitance of the NiMoO$_4$/3D-rGO electrode was estimated to be around 900 Fg^{-1} at 1 A g^{-1}, which is a relatively good result, compared to many other studies; for example, the C/NiMoO$_4$ electrode (859 Fg^{-1} at 1 A g^{-1}) [15], the NiMoO$_4$/CoMoO$_4$ nanorods electrode (1445 Fg^{-1} at 1 A g^{-1}) [16], the CoMoO$_4$–NiMoO$_4 \cdot x$H$_2$O electrode (1039 Fg^{-1} at 2.5 mA cm^{-2}) [21], the NiMoO$_4$ electrode (800 Fg^{-1} at 1 A g^{-1}) [22], and the sphere-shaped NiMoO$_4$ electrode (1000 Fg^{-1} at 1 A g^{-1}) [25].

4. Conclusions

A NiMoO$_4$/3D-rGO nanocomposite was prepared with a simple and effective precipitation method in starch media. This technique is useful for synthesizing a large amount of NiMoO$_4$/3D-rGO nanocomposite for supercapacitor application. The results confirmed the transformation of GO to rGO during the process. The calculated specific capacity of the NiMoO$_4$/3D-rGO and NiMoO$_4$ electrode was 450 Cg^{-1} (900 Fg^{-1}) and 350 Cg^{-1} (700 Fg^{-1}), respectively, at the current density of 1 A g^{-1}. The good specific capacity of the nanocomposite can be attributed to the 3D structure of the rGO sheets and the faradaic reaction of NiMoO$_4$ nanoparticles. This porous structure resulted in rapid electron and ion transportation. Therefore, using starch to produce a porous surface area is recommended to synthesize the nanocomposite of NiMoO$_4$ and rGO for the investigation of hybrid supercapacitor electrodes.

Author Contributions: S.A.R.: Investigation, synthesis, and writing—original draft, R.S.M.: Supervision, N.B.: Editing and formal analysis, M.P.: Software, and H.O.: Supervision and editing manuscript. All authors have read and agreed to the published version of the manuscript.

Funding: This research received no external funding.

Acknowledgments: The authors acknowledge Tarbiat Modares University and Mid Sweden University for providing the facilities and technical assistance for this research. We thank the honorable supervisors, Magnus Hummelgård, and all of the personnel who work in the research.

Conflicts of Interest: The authors declare no conflict of interest.

References

1. Xia, X.; Zhang, Y.; Chao, D.; Guan, C.; Zhang, Y.; Li, L.; Fan, H.J. Solution synthesis of metal oxides for electrochemical energy storage applications. *Nanoscale* **2014**, *6*, 5008–5048. [CrossRef] [PubMed]

2. Iro, Z.S.; Subramani, C.; Dash, S.S. A brief review on electrode materials for supercapacitor. *Int. J. Electrochem. Sci.* **2016**, *11*, 10628–10643. [CrossRef]

3. Budhiraju, V.S.; Kumar, R.; Sharma, A.; Sivakumar, S. Structurally stable hollow mesoporous graphitized carbon nanofibers embedded with NiMoO$_4$ nanoparticles for high performance asymmetric supercapacitors. *Electrochim. Acta* **2017**, *238*, 337–348. [CrossRef]

4. Gund, G.S.; Lokhande, C.D.; Park, H.S. Controlled synthesis of hierarchical nanoflake structure of NiO thin film for supercapacitor application. *Alloys Compd.* **2018**, *741*, 549–556. [CrossRef]

5. Wang, H.; Song, Y.; Liu, W.; Yan, L. Three dimensional Ni(OH)$_2$/rGO hydrogel as binder-free electrode for asymmetric supercapacitor. *Alloys Compd.* **2018**, *735*, 2428–2435. [CrossRef]

6. Liu, F.; Chu, X.; Zhang, H.; Zhang, B.; Su, H.; Jin, L.; Yang, W. Synthesis of self-assembly 3D porous Ni(OH)$_2$ with high capacitance for hybrid supercapacitors. *Electrochim. Acta* **2018**, *269*, 102–110. [CrossRef]

7. Brisse, A.L.; Stevens, P.; Toussaint, G.; Crosnier, O.; Brousse, T. Ni(OH)$_2$ and NiO Based Composites: Battery Type Electrode Materials for Hybrid Supercapacitor Devices. *Materials* **2018**, *11*, 1178. [CrossRef]

8. Chiu, H.Y.; Cho, C.P. Mixed-Phase MnO$_2$/N-Containing Graphene Composites Applied as Electrode Active Materials for Flexible Asymmetric Solid-State Supercapacitors. *Nanomaterials* **2018**, *8*, 924. [CrossRef]

9. Fei, H.; Saha, N.; Kazantseva, N.; Moucka, R.; Cheng, Q.; Saha, P. A highly flexible supercapacitor based on MnO$_2$/RGO nanosheets and bacterial cellulose-filled gel electrolyte. *Materials* **2017**, *10*, 1251. [CrossRef]

10. Prakash, N.G.; Dhananjaya, M.; Narayana, A.L.; Shaik, D.P.; Rosaiah, P.; Hussain, O.M. High Performance One Dimensional α-MoO$_3$ Nanorods for Supercapacitor Applications. *Ceram. Int.* **2018**, *44*, 9967–9975. [CrossRef]

11. Zhang, H.; Zhou, Y.; Ma, Y.; Yao, J.; Li, X.; Sun, Y.; Li, D. RF magnetron sputtering synthesis of three-dimensional graphene@Co$_3$O$_4$ nanowire array grown on Ni foam for application in supercapacitors. *Alloys Compd.* **2018**, *740*, 174–179. [CrossRef]

12. Zhao, J.; Li, Z.; Yuan, X.; Yang, Z.; Zhang, M.; Meng, A.; Li, Q. A High-Energy Density Asymmetric Supercapacitor Based on Fe_2O_3 Nanoneedle Arrays and $NiCo_2O_4$/$Ni(OH)_2$ Hybrid Nanosheet Arrays Grown on SiC Nanowire Networks as Free-Standing Advanced Electrodes. *Adv. Energy Mater.* **2018**, *8*, 1702787–1702791. [CrossRef]

13. Zhang, C.; Lei, C.; Cen, C.; Tang, S.; Deng, M.; Li, Y.; Du, Y. Interface polarization matters: Enhancing supercapacitor performance of spinel $NiCo_2O_4$ nanowires by reduced graphene oxide coating. *Electrochim. Acta* **2018**, *260*, 814–822. [CrossRef]

14. Umapathy, V.; Neeraja, P.; Manikandan, A.; Ramu, P. Synthesis of $NiMoO_4$ nanoparticles by sol–gel method and their structural, morphological, optical, magnetic and photocatlytic properties. *Trans. Nonferrous Met. Soc. China* **2017**, *27*, 1785–1793. [CrossRef]

15. Xuan, H.; Xu, Y.; Zhang, Y.; Li, H.; Han, P.; Du, Y. One-step combustion synthesis of porous CNTs/C/$NiMoO_4$ composites for high-performance asymmetric supercapacitors. *Alloys Compd.* **2018**, *745*, 135–146. [CrossRef]

16. Nti, F.; Anang, D.A.; Han, J.I. Facilely synthesized $NiMoO_4$/$CoMoO_4$ nanorods as electrode material for high performance supercapacitor. *Alloys Compd.* **2018**, *742*, 342–350. [CrossRef]

17. Yesuraj, J.; Elumalai, V.; Bhagavathiachari, M.; Samuel, A.S.; Elaiyappillai, E.; Johnson, P.M. A facile sonochemical assisted synthesis of α-$MnMoO_4$/PANI nanocomposite electrode for supercapacitor applications. *Electroanal. Chem.* **2017**, *797*, 78–88. [CrossRef]

18. Xiao, K.; Xia, L.; Liu, G.; Wang, S.; Ding, L.X.; Wang, H. Honeycomb-like $NiMoO_4$ ultrathin nanosheet arrays for high-performance electrochemical energy storage. *J. Mater. Chem. A* **2015**, *3*, 6128–6135. [CrossRef]

19. Xiong, X.; Ding, D.; Chen, D.; Waller, G.; Bu, Y.; Wang, Z.; Liu, M. Three-dimensional ultrathin $Ni(OH)_2$ nanosheets grown on nickel foam for high-performance supercapacitors. *Nano. Energy* **2015**, *11*, 154–161. [CrossRef]

20. Mohapatra, D.; Parida, S.; Singh, B.K.; Sutar, D.S. Importance of microstructure and interface in designing metal oxide nanocomposites for supercapacitor electrodes. *Electroanal. Chem.* **2017**, *803*, 30–39. [CrossRef]

21. Liu, M.C.; Kong, L.B.; Lu, C.; Ma, X.J.; Li, X.M.; Luo, Y.C.; Kang, L. Design and synthesis of $CoMoO_4$–$NiMoO_4 \cdot xH_2O$ bundles with improved electrochemical properties for supercapacitors. *J. Mater. Chem. A* **2013**, *1*, 1380–1387. [CrossRef]

22. Liu, T.; Chai, H.; Jia, D.; Su, Y.; Wang, T.; Zhou, W. Rapid microwave-assisted synthesis of mesoporous $NiMoO_4$ nanorod/reduced graphene oxide composites for high-performance supercapacitors. *Electrochim. Acta* **2015**, *180*, 998–1006. [CrossRef]

23. Kianpour, G.; Salavati-Niasari, M.; Emadi, H. Sonochemical synthesis and characterization of $NiMoO_4$ nanorods. *Ultrason. Sonochem.* **2013**, *20*, 418–424. [CrossRef] [PubMed]

24. De Moura, A.P.; de Oliveira, L.H.; Rosa, I.L.; Xavier, C.S.; Lisboa-Filho, P.N.; Li, M.S.; Varela, J.A. Structural, optical, and magnetic properties of $NiMoO_4$ nanorods prepared by microwave sintering. *Sci. World J.* **2015**, *1*, 1–9. [CrossRef]

25. Jinlong, L.; Miura, H.; Meng, Y. A novel mesoporous $NiMoO_4$@rGO nanostructure for supercapacitor applications. *Mater. Lett.* **2017**, *194*, 94–97. [CrossRef]

26. Arshadi Rastabi, S.; Sarraf Mamoory, R.; Dabir, F.; Blomquist, N.; Phadatare, M.; Olin, H. Synthesis of $NiMoO_4$/3D-rGO Nanocomposite in Alkaline Environments for Supercapacitor Electrodes. *Crystals* **2019**, *9*, 31. [CrossRef]

27. Kumar, Y.; Kim, H.J. Effect of Time on a Hierarchical Corn Skeleton-Like Composite of CoO@ZnO as Capacitive Electrode Material for High Specific Performance Supercapacitors. *Energies* **2018**, *11*, 3285. [CrossRef]

28. Ossonon, B.D.; Bélanger, D. Synthesis and characterization of sulfophenyl-functionalized reduced graphene oxide sheets. *RSC Adv.* **2017**, *7*, 27224–27234. [CrossRef]

29. Srivastava, M.; Uddin, M.E.; Singh, J.; Kim, N.H.; Lee, J.H. Preparation and characterization of self-assembled layer by layer $NiCo_2O_4$–reduced graphene oxide nanocomposite with improved electrocatalytic properties. *Alloys Compd.* **2014**, *590*, 266–276. [CrossRef]

30. Fayer, M.D. *Ultrafast Infrared Vibrational Spectroscopy*; CRC Press: New York, NY, USA, 2013; Volume 4, p. 128.

31. Li, Y.; Jian, J.; Fan, Y.; Wang, H.; Yu, L.; Cheng, G.; Sun, M. Facile one-pot synthesis of a $NiMoO_4$/reduced graphene oxide composite as a pseudocapacitor with superior performance. *RSC Adv.* **2016**, *6*, 69627–69633. [CrossRef]

32.　Bankar, P.K.; Ratha, S.; More, M.A.; Late, D.J.; Rout, C.S. Enhanced field emission performance of NiMoO$_4$ nanosheets by tuning the phase. *Appl. Surf. Sci.* **2017**, *418*, 270–274. [CrossRef]

33.　Ezeigwe, E.R.; Khiew, P.S.; Siong, C.W.; Tan, M.T. Synthesis of NiMoO$_4$ nanorods on graphene and superior electrochemical performance of the resulting ternary based composites. *Ceram. Int.* **2017**, *43*, 13772–13780. [CrossRef]

34.　Azarang, M.; Shuhaimi, A.; Yousefi, R.; Sookhakian, M. Effects of graphene oxide concentration on optical properties of ZnO/RGO nanocomposites and their application to photocurrent generation. *Appl. Phys.* **2014**, *116*, 84307–84313. [CrossRef]

35.　Jamali-Sheini, F.; Azarang, M. Effect of annealing temperature and graphene concentrations on photovoltaic and NIR-detector applications of PbS/rGO nanocomposites. *Ceram. Int.* **2016**, *42*, 15209–15216. [CrossRef]

36.　Uddin, A.S.M.I.; Phan, D.T.; Chung, G.S. Synthesis of ZnO nanoparticles-reduced graphene oxide composites and their intrinsic gas sensing properties. *Surf. Rev. Lett.* **2014**, *21*, 1450086–1450097. [CrossRef]

37.　Guan, X.H.; Lan, X.; Lv, X.; Yang, L.; Wang, G.S. Synthesis of NiMoSO/rGO Composites Based on NiMoO$_4$ and Reduced Graphene with High-Performance Electrochemical Electrodes. *ChemistrySelect* **2018**, *3*, 6719–6728. [CrossRef]

38.　Jothi, P.R.; Kannan, S.; Velayutham, G. Enhanced methanol electro-oxidation over in-situ carbon and graphene supported one dimensional NiMoO$_4$ nanorods. *J. Power Sources* **2015**, *277*, 350–359. [CrossRef]

39.　Ghosh, D.; Giri, S.; Das, C.K. Synthesis, characterization and electrochemical performance of graphene decorated with 1D NiMoO$_4$·nH$_2$O nanorods. *Nanoscale* **2013**, *5*, 10428–10437. [CrossRef]

40.　Jothi, P.R.; Shanthi, K.; Salunkhe, R.R.; Pramanik, M.; Malgras, V.; Alshehri, S.M.; Yamauchi, Y. Synthesis and Characterization of α-NiMoO$_4$ Nanorods for Supercapacitor Application. *Eur. J. Inorg. Chem.* **2015**, *22*, 3694–3699. [CrossRef]

41.　Liu, H.; Zhang, G.; Zhou, Y.; Gao, M.; Yang, F. One-step potentiodynamic synthesis of poly (1,5-diaminoanthraquinone)/reduced graphene oxide nanohybrid with improved electrocatalytic activity. *J. Mater. Chem. A* **2013**, *1*, 13902–13913. [CrossRef]

42.　Li, Y.; Jian, J.; Xiao, L.; Wang, H.; Yu, L.; Cheng, G.; Sun, M. Synthesis of NiMoO$_4$ nanosheets on graphene sheets as advanced supercapacitor electrode materials. *Mater. Lett.* **2016**, *184*, 21–24. [CrossRef]

43.　Trafela, Š.; Zavašnik, J.; Šturm, S.; Rožman, K.Ž. Formation of a Ni(OH)$_2$/NiOOH active redox couple on nickel nanowires for formaldehyde detection in alkaline media. *Electrochim. Acta* **2019**, *309*, 346–353. [CrossRef]

44.　Jiang, G.; Zhang, M.; Li, X.; Gao, H. NiMoO$_4$@Ni(OH)$_2$ core/shell nanorods supported on Ni foam for high-performance supercapacitors. *RSC Adv.* **2015**, *85*, 69365–69370. [CrossRef]

45.　Yedluri, A.K.; Anitha, T.; Kim, H.J. Fabrication of Hierarchical NiMoO$_4$/NiMoO$_4$ Nanoflowers on Highly Conductive Flexible Nickel Foam Substrate as a Capacitive Electrode Material for Supercapacitors with Enhanced Electrochemical Performance. *Energies* **2019**, *12*, 1143. [CrossRef]